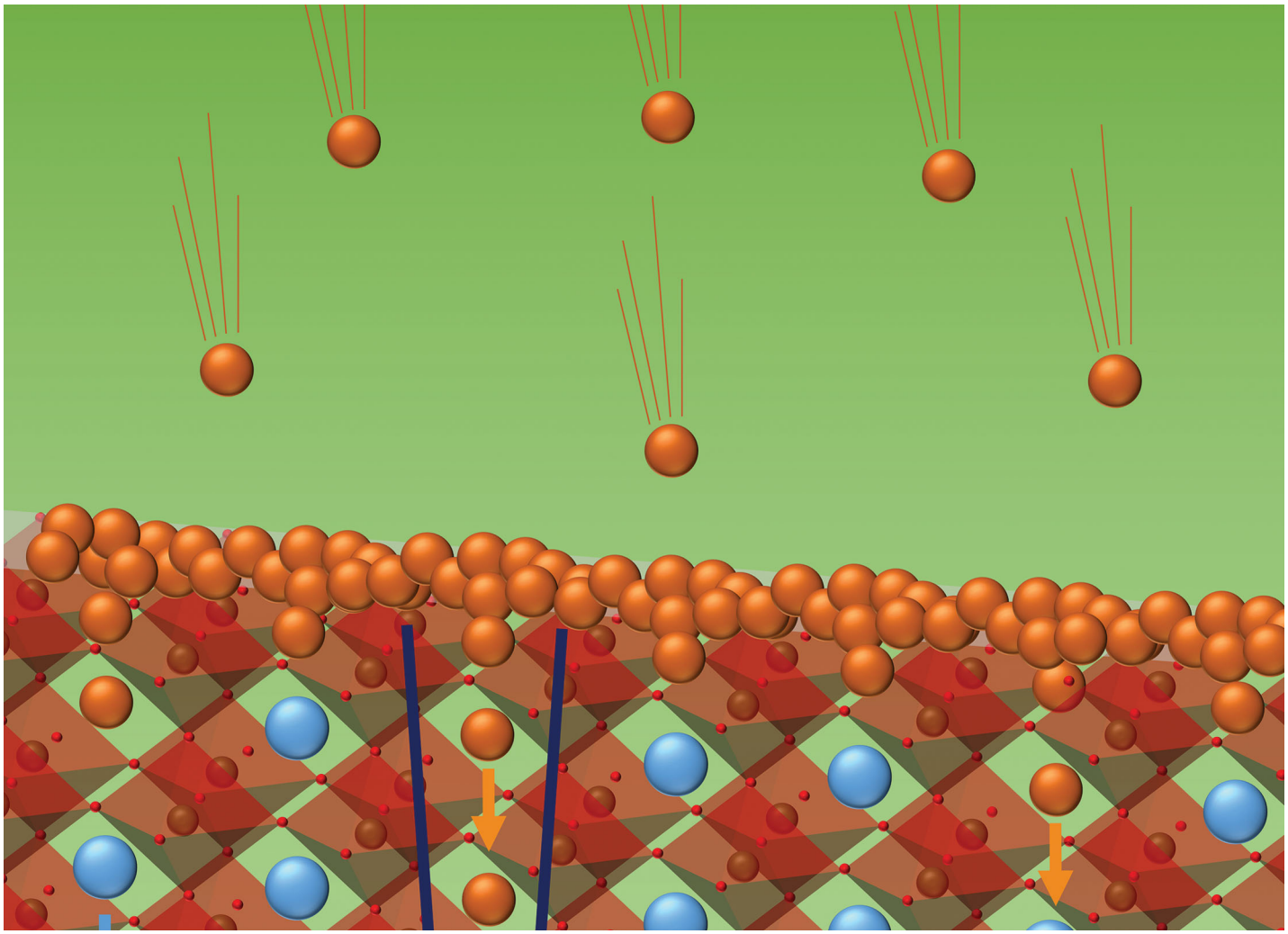

Showcasing research from the laboratories of Prof. Karl-Michael Weitzel at the Philipps-Universität Marburg, Germany, Prof. Christian Jooss, Universität Göttingen, Germany and Prof. Katsuyo Thornton, University of Michigan, USA.

Charge attachment induced transport – bulk and grain boundary diffusion of potassium in $PrMnO_3$

The attachment of potassium ions to the surface of electronically conductive $PrMnO_3$ leads to the deposition of a K layer. The gradient of the concentration of K induced by this causes the transport of K though the thin film sample. Quantitative analysis of the concentration profiles by means of TOF-SIMS combined with theoretical model calculations allows demonstration of the competition between bulk and grain boundary diffusion. These grain boundaries are also evidenced by high-resolution FIB-TEM images. K appears to replace Pr in the A sites of the perovskite $PrMnO_3$.

As featured in:

See Karl-Michael Weitzel *et al.*, *Phys. Chem. Chem. Phys.*, 2017, **19**, 9762.

ROYAL SOCIETY OF CHEMISTRY

rsc.li/pccp

Registered charity number: 207890

PCCP

PAPER

View Article Online
View Journal | View Issue

Cite this: *Phys. Chem. Chem. Phys.*, 2017, **19**, 9762

Charge attachment induced transport – bulk and grain boundary diffusion of potassium in $PrMnO_3$†

Johannes Martin,[a] Melanie Gräf,[a] Thilo Kramer,[b] Christian Jooss,[b] Min-Ju Choe,[c] Katsuyo Thornton[c] and Karl-Michael Weitzel*[a]

Received 10th January 2017,
Accepted 1st March 2017

DOI: 10.1039/c7cp00198c

rsc.li/pccp

The transport of potassium through praseodymium-manganese oxide ($PrMnO_3$; PMO) has been investigated by means of the charge attachment induced transport (CAIT) technique. To this end, potassium ions have been attached to the front side of a 250 nm thick sample of PMO. The majority of the potassium ions become neutralized at the surface of the PMO, while some of the potassium ions diffuse through. *Ex situ* analysis of the sample by time-of-flight secondary ion mass spectrometry (ToF-SIMS) reveals pronounced concentration profiles of the potassium, which is indicative of diffusion. Two diffusion coefficients have been obtained, namely, the bulk diffusion coefficient and the diffusion coefficient associated with the grain boundaries. The latter conclusion is supported by transmission electron microscopy of thin lamella cut out from the sample, which reveals twin grain boundaries reaching throughout the entire sample as well as model calculations.

1 Introduction

Perovskite-oxide based materials with the composition ABO_3 have promising potential for new innovations and technologies including solid oxide fuel cells (SOFC),[1] water electrolysis,[2,3] and resistive random access memory (RRAM).[4,5] Operating temperatures for these devices can range from room temperature (*e.g.*, water electrolysis electrodes[2,6]) to high temperatures (*e.g.*, SOFC and RRAM). Therefore, an understanding of ionic mobility and diffusion over a wide temperature range is necessary.

The perovskite oxide ABO_3 structure consists of a network of corner sharing BO_6 octahedra, while A-site cations exhibit dodecahedral environments to next neighbor oxygen. The large A-site cations stabilize the crystal structure of perovskite oxides, enabling the accommodation of high point defect concentrations, *e.g.* in $La_{1-x}Sr_xCoO_{3-\delta}$[7] and $La_{1-x}Sr_xMnO_{3-\delta}$.[8] These high defect concentrations give rise to a large variety of physical effects including conduction phenomena connected to electron and hole doping, *e.g.* in $La_{1-x}A_xMnO_3$ (A = Ca or Ce),[9] and the colossal magneto resistance in hole doped manganites.[10] High temperature tracer diffusion data compiled by Miyoshi *et al.* for cations in $LaMnO_3$ and by Ishigaki *et al.* for anions in strontium doped $LaMnO_3$, show a trend in which the diffusion of oxygen is faster than that of manganese, which is in turn faster than that of praseodymium.[11] The relative value of diffusion coefficients of A-site and B-site cations can differ by many orders of magnitude and, as a result, significantly influence the surface and interface chemistry and dopant concentrations under operation. Thus, it is particularly important to obtain information about the relative values, but there seems to be no general trend. One important contribution to a better understanding is extending diffusion data of different cation and anion species to room temperature. For manganites, which represent mixed ionic–electronic conductors, this requires a highly sensitive and reliable method.

In a series of papers published in this journal we have described the development and selected applications of the "*Bombardment Induced Ion Transport*" technique.[12–16] That work was based on attaching an alkali ion beam of well-defined energy to a sample of interest. If the sample has a low conductivity, attachment of ions will lead to charging the surface. This in turn generates gradients of the electric potential and the concentration towards a backside electrode. Measurements of current–voltage data then provides direct access to the conductivity. When the bombarder ion is different from the native conducting ion, concentration profiles evolve, which are classified as electrodiffusion profiles, since they contain contributions from migration and diffusion.[17,18]

In this work, we present an extension of the approach described above to investigate potassium diffusion in a praseodymium-manganese oxide with the composition $PrMnO_3$ (PMO). To this end, a low-energy K^+ beam is aimed at a PMO sample in contact

[a] *Fachbereich Chemie, Philipps-Universität Marburg, Marburg, Germany. E-mail: weitzel@chemie.uni-marburg.de*
[b] *Institut für Materialphysik, Georg-August-Universität Göttingen, Göttingen, Germany*
[c] *Department of Materials Science & Engineering, University of Michigan, Ann Arbor, USA*

† Electronic supplementary information (ESI) available. See DOI: 10.1039/c7cp00198c

with a single platinum electrode. Since the PMO exhibits a relatively low electrical resistivity ($\approx$100 Ω cm) due to negative charge carriers, the sample surface will not become charged in this case. However, pronounced concentration gradients will develop and induce diffusion. This constitutes Charge Attachment Induced Transport (CAIT) in the sample. Ultimately, the transport of potassium through the PMO gives rise to concentration profiles characteristic of diffusion. The concentration profiles will be quantitatively determined by means of time-of-flight secondary ion mass spectrometry (ToF-SIMS) and rationalized by theoretical modeling. A high-resolution transmission electron microscope (TEM) and an energy-dispersive X-ray spectroscopy (EDX) are used to support the central findings of the ToF-SIMS analysis. The perovskite structure of the PMO is maintained, even near the interface of the potassium surface layer.

2 Materials and methods

2.1 Sample preparation

The samples were deposited by ion beam sputtering technique on 10 × 10 mm MgO[001] single crystal substrates. First, about 600 nm of Pt as bottom electrode followed by 250 nm of PMO are deposited at 1023 K under 1.4×10^{-4} mbar O_2, 1.0×10^{-4} mbar Xe (sputter gas) and 1.0×10^{-4} mbar Ar (neutralizer plasma) background pressure. In order to have a well-defined area for the charge attachment experiment, a ring of 8 mm diameter Allresist AR_N 7520.18 negative lacquer was prepared on the PMO by electron beam lithography. The sample was glued to a copper electrode by using thermally and electrically conductive glue (*Polytech EC 101*). The platinum layer and the copper electrode were short-circuited by means of a copper mesh glued on both materials.

2.2 Charge attachment induced transport

The basic concept of the experimental approach has been described in previous reports.[13,18,19] Only a brief summary of the important key features is given in this section. The setup can be divided into three parts: (i) the generation of ions, (ii) the guiding of ions and (iii) the sample region. Alkali containing tectosilicates with the common composition $MAlSi_2O_6$ (here M: K) were synthesized in the lab and used to generate these M^+ ions *via* the thermionic emission. The synthesis and properties of these ion sources have been presented elsewhere.[20] To guarantee a collision free path of the K^+ ion to the sample, the working pressure was set to a value below 2×10^{-6} mbar. The ion source was operated at a working temperature of about 1148 K and a fixed potential of 10 V, applied at the repeller lens to accelerate the ions towards the sample. The potential applied to the abstraction lens was −1.90 kV, so that the electric field relevant for thermionic emission was -2 kV cm^{-1}. The current of the ion beam I_{Ref} was $\geq$200 nA. The potassium ions were guided and focused towards the sample *via* ion optics consisting of a system of electrostatic lenses. The ions were passed through a grounded aperture with three 95%-transmission meshes inside. The middle mesh was used to record the reference current, while the two outer meshes guaranteed homogeneous electric fields in front of the middle mesh and in front of the sample, respectively. After passing the aperture, the ions reach the sample surface. The bombarded area was determined by a steel mask placed 1 mm from the surface of the PMO (and thus not in contact). This setup is similar to that described in ref. 19, with the exception that the mask was in contact with the sample in that work. Since the PMO is a good electrical conductor[21,22] for negative charge carriers (electrons and possibly O^{2-} ions), the ions were neutralized upon adsorption at its surface. The deposition of potassium leads to a concentration gradient at the front interface of the sample such that transport in the sample was induced. The current through the PMO, I_{back}, was recorded with a homemade transimpedance-amplifier, A/D converted, and processed in a computer. The measurement was completed when the incorporated amount of ions reached a charge of 10 mC. The sample temperature was set to 308.15 K and kept constant to $\pm$0.1 K *via* a resistance heating device equipped with a Pt100 thermometer and a temperature controller (Series 3216, *Eurotherm*).

2.3 Depth profiling

Concentration profiles arising from diffusion of potassium through the sample are analyzed by ToF-SIMS[5] (IONTOF GmbH, Münster, Germany). For analysis of positive ions, the Bi^+-LMIG (liquid metal ion gun) is used in the high current bunched mode (25 keV Bi^+-ions, pulsed target current 0.50 pA). A Cs^+ ion gun (30 nA; 3 kV) and an O_2^+ ion gun (150 nA; 3 kV) are used for the sputtering process. The reason for using two different sputter guns will be discussed in the results section. All ion guns are oriented at a 45° angle to the sample surface. The area analyzed by the LMIG is 100 μm × 100 μm with a resolution of (128 × 128) pixels in the interlaced mode. The sputtered area was 300 μm × 300 μm. Mass spectra were collected within the mass range up to the mass to charge ratio of m/z = 800 with a mass resolution of $m/\Delta m$ = 6000–8000. The SIMS spectra are calibrated using the peaks with a well-known mass to charge ratio, *e.g.*, potassium ($^{39}K^+$, $^{41}K^+$), manganese (Mn^+) or praseodymium (Pr^+). With this technique, about 10^7 mass spectra are recorded per crater, giving access to concentration profiles. The integrated area of the investigated ion peaks is obtained as a function of sputter time. The crater depth is determined post-analysis with a surface profilometer (SLOAN Dektak3ST, Veeco Instruments) and TEM to translate the sputter time into a sputter depth.

2.4 Electron microscopy

Changes of the microstructure and chemical structure due to ion incorporation on the nm scale are studied by transmission electron microscopy (TEM). We have used an aberration corrected FEI TITAN ETEM 80–300 with 300 kV acceleration voltage and a Philips CM 12 with 120 kV acceleration voltage, both equipped with an energy dispersive X-ray (EDX) detection system (X-Max provided by Oxford instruments with 130 eV energy resolution). EDX line scans were measured in scanning mode (STEM) with a spatial resolution of about 5 nm (CM12) or about 1 nm (TITAN). For the preparation of electron transparent thin lamellas, a

focused ion beam (FIB) system (FEI Nova NanoLab 600; dual beam) is used. It is equipped with a gas injection system that enables chemical vapor deposition of carbon-platinum protection layers (hereafter termed FIB-Pt) using a carbon-platinum precursor. In addition, scanning electron microscope (SEM) images of the sample surfaces after ion incorporation are acquired by this system. Before every TEM lamella preparation, a protection layer of about 1 μm FIB-Pt is deposited in two steps in the respective area, cracking the precursor first with a 5 kV/1.6 nA electron beam and then a 30 kV/300 pA Ga^+-ion beam. For the lamella cut out and thinning we have used a 30 kV Ga^+-beam with beam currents between 30 pA and 7 nA.

3 Results

The diffusion of potassium through PMO has been investigated by the CAIT approach. A low energy K^+ ion beam (E_{kin} = 10 eV) was incident on the PMO sample for 28.3 hours, inducing the attachment of K^+ corresponding to a charge of 10 mC. During the bombardment, the measured backside current was constant (about 98 nA ± 7 nA) and the estimated reference current, I_{Ref}, obtained from a current measurement at the 95% transmission mesh was ≥200 nA. The sample temperature was kept constant at T = 308.15 K. Directly after finishing the CAIT experiment, the sample was transferred to a ToF-SIMS machine where a depth profiling was performed. These concentration profiles clearly exhibited a pronounced diffusion profile of the potassium in the PMO sample. These concentration profiles will be analyzed and discussed below. Subsequent to the ToF-SIMS analysis, the sample was also analyzed by means of SEM and TEM.

3.1 ToF-SIMS analysis – data processing and interpretation

In ToF-SIMS, the raw data (provided as ESI†) are affected by different detection efficiencies for distinct elements.[16] For quantitative analysis, the raw data must be normalized to take into account such variation as well as the stoichiometry of the sample. Inside the bulk of the PMO, the molar fractions x_i^0 of O^+, Mn^+ and Pr^+ are well known. The averaged ion signal between the depth of 100 nm and 200 nm is related to the molar fraction of the corresponding ion by using eqn (1),

$$x_i^0 = \frac{n_i^0}{n_{O^+}^0 + n_{Mn^+}^0 + n_{Pr^+}^0} = a_i \cdot I_i, \quad \text{with } i = O^+, Mn^+, Pr^+, \tag{1}$$

where n is the amount of substance, a is a proportionality constant, and I is the ToF-SIMS signal. The averaged platinum ion signal in its bulk between the depth of 400 nm and 420 nm and the highest potassium ion signal at the onset of the PMO are set to be one. It should be noted that the potassium ion signal in the vicinity of the surface (first 3 nm) is ignored due to the transient effect in SIMS.[23,24] Finally, for graphical presentation, the concentration profiles for oxygen and platinum have been averaged over five data points in the depth domain. The final concentration profiles derived from this ToF-SIMS analysis of the PMO bombarded with potassium ions is shown in Fig. 1. The Cs^+ gun has been used for sputtering in this analysis.

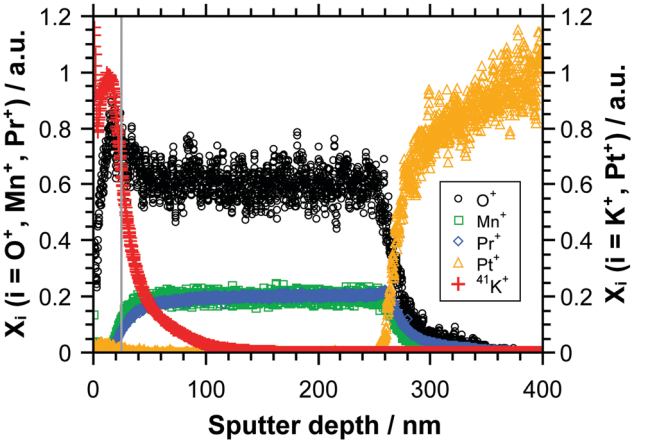

Fig. 1 Concentration profile of the bombarded $PrMnO_3$. The ion signals are normalized to their molar fraction.

Within the first nm, only the potassium signal (red crosses) and the oxygen signal (black circles) are observed. Subsequently the manganese signal (green squares) and the praseodymium signal (blue diamonds) increases. The front edge of the PMO is determined by the inflection point of the manganese signal marked by the grey solid line at 25 nm. The cesium sputtering causes a signal at m/z (Cs_2O^{++}) = 140.905, which interferes with the praseodymium ion signal at m/z (Pr^+ = 140.908). Therefore, for the data displayed in Fig. 1, we have used the PrO^+ ion signal instead of the Pr^+ signal to represent the praseodymium concentration profile. This procedure has been validated by performing ToF-SIMS depth profiling on a reference PMO sample employing an O_2^+ sputter gun. These studies demonstrate that an apparent Pr^+ peak observable in the raw data at the PMO–platinum interface for Cs^+ sputtering does not occur for O_2^+ sputtering (for further details see ESI†). It is therefore justified to label the PrO^+ trace "Pr^+". Furthermore, the intensity of the $^{39}K^+$-ion signal is often so strong that it saturates the detector. We therefore use the $^{41}K^+$-ion signal to represent the potassium concentration instead.

The potassium ion signal as well as the oxygen ion signal show a local maximum in the intensity around 17 nm. Additionally it is observed that, inside the PMO matrix, the oxygen ion signal decreases. It is well known that the oxygen ions are mobile, due to the oxygen vacancy-related transport mechanism in perovskite typed materials.[25–27] Consequently, one might expect that oxygen ions diffuse in the direction of the PMO surface due to the chemical potential that is generated by the adsorbed potassium ions. In doped $La_{0.8}Sr_{0.2}MnO_3$ $^{18}O/^{16}O$ isotope exchange depth profile experiments at a sample temperature of 700 °C have shown that the diffusion coefficient for oxygen ions is 3.1 × 10^{-16} cm^2 s^{-1}.[28] In our experiment the undoped $PrMnO_3$ has less oxygen vacancies and the sample temperature was set to 35 °C; therefore the oxygen diffusion coefficient is expected to be orders of magnitudes lower. Within the short attachment time of 28.3 h, oxygen diffusion would not be observed. It is more likely that potassium ions are

neutralized at the PMO surface, due to its good electronic conductivity. Later upon transferring the sample to the ToF-SIMS machine, the potassium can possibly react with oxygen to form K_2O or with air humidity to form KOH. Since the profiling is conducted immediately after transferring the sample, this will not affect the concentration profiles inside the PMO region. Fig. 1 illustrates that the potassium is not only deposited at the PMO surface, but also transported into the PMO matrix. One can observe that the potassium signal is decreasing exponentially. Since the potassium is able to occupy praseodymium-sites,[21] the observed behavior could be explained by the substitution of praseodymium by the incorporated potassium. A more detailed analysis shows that the Pr^+ signal slightly increases from the front to the back side of the sample. The effect is small but appears to be reproducible, suggesting that praseodymium is depleted towards the back side and possibly replaced by potassium. This is further supported by the observation that the sum of the normalized Pr^+ and K^+ signals is constant in the bulk region (see data provided in the ESI†). However, further studies are required to better understand which sites are involved in the transport of potassium.

3.2 Electron microscopy

In addition to the SIMS characterization, the sample was examined by electron microscopy. A cross sectional TEM lamella reveals a layer deposited in front of the PMO by the charge attachment experiment (Fig. 2A). The average thickness of this layer is about 30 nm. Fig. 2A also shows that this layer has turned into an agglomeration in one location. An EDX line scan recorded at the position of an agglomerate reveals that this agglomerate consists of potassium and oxygen – as does the entire front layer – (Fig. 2B), which is in good agreement with the SIMS results. The exact stoichiometry of the front layer cannot be determined because of an intermixing with the FIB-platinum protection layer required for the preparation. Most likely, this is also the origin of an unexpected potassium signal within the protection layer. The offset between manganese and praseodymium in Fig. 2B is a systematic error of the EDX analysis. The expected 1 : 1 ratio, however, is measured in the SIMS analysis (Fig. 1). Apart from this discrepancy, the EDX analysis matches well to the SIMS measurements. Fig. 2C and D show STEM images of the PMO–K_xO_y interface being very smooth. STEM EDX line scans across this interface reveal diffusion of the potassium into the PMO sample (Fig. 2E). For a quantitative analysis of the potassium diffusion profile, we will focus on the ToF-SIMS data that have the advantage of sampling over a macroscopic region. Furthermore, this was recorded directly after the transport experiment.

The agglomerations observed in the TEM images (Fig. 2A) are on the average 2 μm wide. At the time of the TEM investigation they covered about 10% of the surface. Most likely, they have

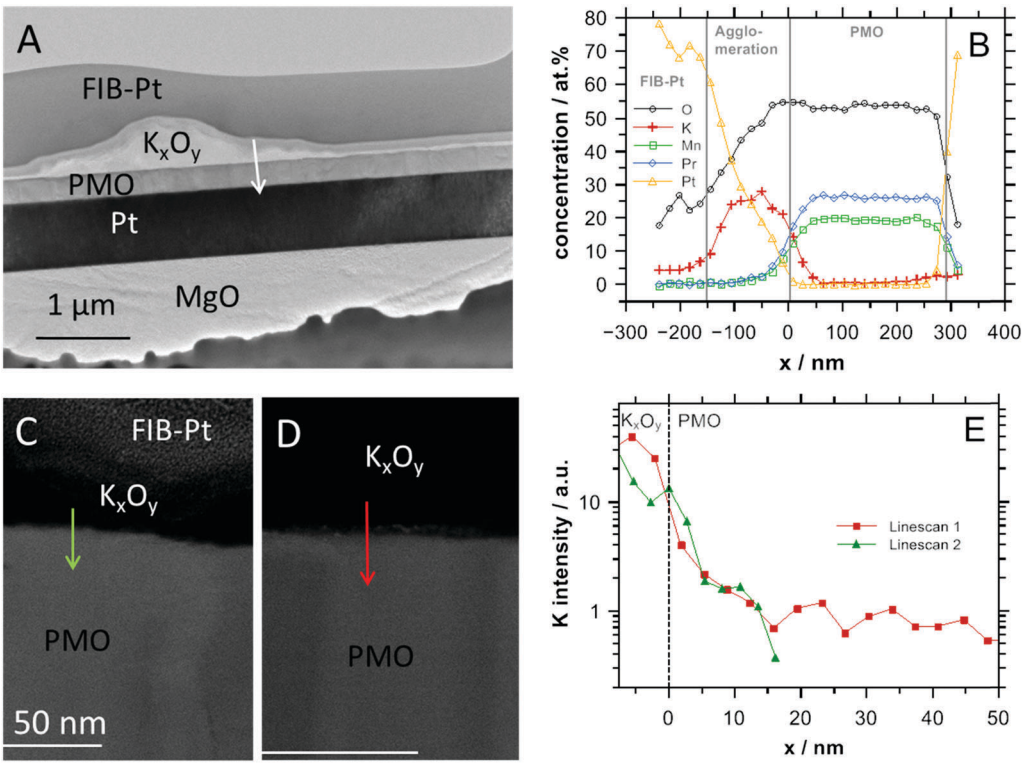

Fig. 2 (A) Cross section TEM image without contrast aperture. The arrows marks the position of the STEM-EDX line scan presented in (B). (B) EDX concentration profile over an agglomeration and the underlying PMO film. The position of the interface of potassium compound and PMO is derived from the manganese signal and set to zero. *x* is the direction orthogonal to the sample surface. (C and D) STEM HAADF images of the interface of PMO to K_xO_y. The arrows mark the location of the EDX potassium profiles presented in (E). (E) STEM-EDX intensity of potassium Kα at the interface of PMO to K_xO_y.

formed after the ToF-SIMS analysis. Evidence for this comes from a thorough analysis of the ToF-SIMS data. Since ToF-SIMS is a surface conformal technique, any relevant agglomerate sitting on the top of the sample would inevitably lead to a shift in the signal characterizing the beginning of the sample, here praseodymium and manganese. No shift is observed in the analysis. The normalized signals of praseodymium, of manganese as well as of potassium are independent of the local position on the ToF-SIMS crater. We further point out, that the TEM data show no positional correlation between the agglomerates and the grain boundaries discussed below.

3.3 Diffusion of potassium in the PMO

The concentration profiles shown in Fig. 1 demonstrate that potassium has been transported into the PMO sample. In the following, we analyze this potassium concentration profile in more detail. Fig. 5 shows the ToF-SIMS signal of potassium (normalized at $\approx$15 nm) as a function of the depth, x, into the PMO. This ToF-SIMS signal is averaged over an area of 100 μm × 100 μm, in contrast to the EDX line scans shown in Fig. 2. We take cautions in interpreting the ToF-SIMS signals in the first 10 nm due to limitations of the technique. Beyond a depth of about 15 nm we assume the potassium ion signal to be proportional to the ion concentration. The obtained ToF-SIMS profile represents a concentration profile that can be compared to theoretical models.

From comparison with previous BIIT work[17,18] it is evident that this profile is not an electrodiffusion profile. One might expect that the potassium profile can be rationalized by a solution of Fick's second representing bulk diffusion. Here, we are constantly shining a potassium ion beam at the sample surface constituting in good approximation a constant source. As we will further elucidate below the experimental concentration profiles cannot be rationalized by assuming a single pathway of bulk diffusion. This raised the question of whether two different transport pathways may be operative.

To shed further light on this question we have recorded additional high-resolution TEM images. The TEM-data (Fig. 3) reveal that the film has a columnar structure, which is caused by the existence of twin boundaries between (001) and (110) oriented twin domains. Here, the columns are separated by twin boundaries with an average distance of about 140 nm. The reason for this structure may be from a ferroelastic transition from cubic to orthorhombic narrowly below the deposition temperature[29] which leads to different twin orientations. This suggests two possible pathways for the potassium ion transport: (i) the bulk diffusion path and (ii) the diffusion along the twin boundaries.

Generally, diffusion along the grain boundary is much faster than the bulk diffusion.[30] It has not been possible to observe concentration profiles along the grain boundaries in STEM-EDX, possibly due to the relatively high diffusion coefficient in combination with the time of several months between bombardment, lamella preparation, and increased temperatures during the latter. However, the STEM-EDX data (Fig. 2E) in the bulk shows profiles as expected according to Fig. 5 for bulk diffusion.

The experimental concentration profile of potassium can be approximated by Fisher's model and lends support to the conclusion that the transport is dominated by the concentration gradient of potassium. In our theoretical modeling we examine the free diffusion of potassium in PMO from $\approx$15 nm (of the sputter depth) using a simulation configuration similar to that used by Fisher.[31] The equations for bulk and grain boundary diffusion are discretized using the finite difference method as described in ref. 32. The computational domain contains 141 × 245 grid points in the x and y directions, respectively, which is bisected vertically with a straight grain boundary. These dimensions represent the average distance between grain boundaries and free diffusion distance, respectively.

For the boundary conditions, constant values of one and zero are imposed at $y = 0$ and $y = 246$, respectively. This is assuming a constant source of potassium and that the opposite face is far from the deposited surface. We impose periodic boundary conditions on the remaining two edges. This configuration represents the experimental sample where twin boundaries are an average distance of 140 nm apart. Fig. 4 compares the concentration profile between mixed pathway transport with

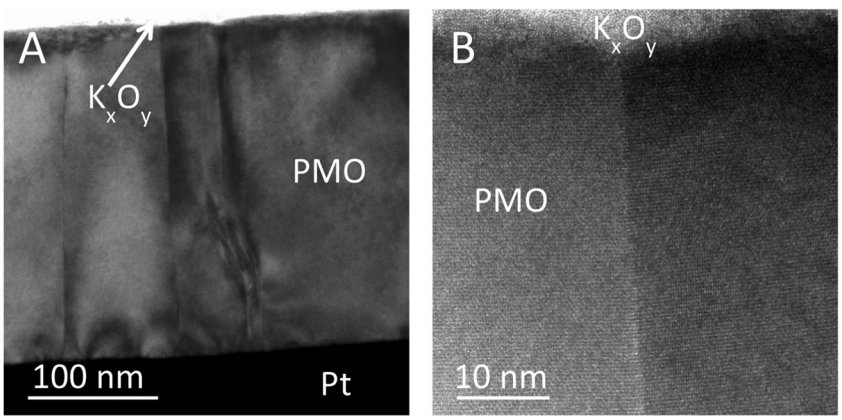

Fig. 3 (A) TEM Bright field image of the PMO film with representative density of twin boundaries (B) HRTEM image of a section of a twin boundary close to the surface.

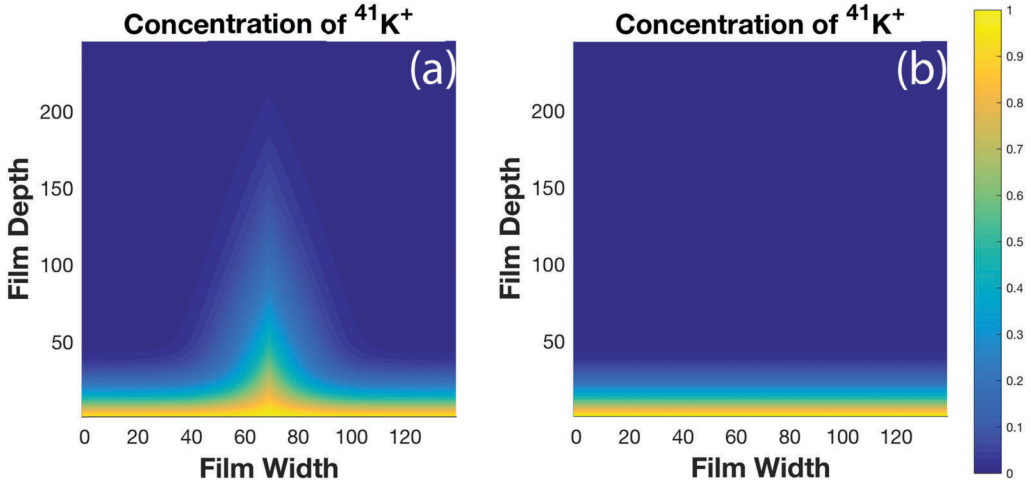

Fig. 4 Simulated concentration distributions using Fisher's model for (a) mixed pathway diffusion with enhanced grain boundary diffusion where D_b = 1.5 × 10^{-17} cm^2 s^{-1} and D_{gb} = 2.5 × 10^{-14} cm^2 s^{-1} and (b) bulk diffusion only where D_b = 1.5 × 10^{-17} cm^2 s^{-1}.

enhanced grain boundary diffusion (Fig. 4a) and uniform diffusion in the bulk only (Fig. 4b) at t = 102 000 seconds (28.4 hours). Fig. 5 plots the average concentration along the film thickness for both simulation configurations along with the experimental ToF-SIMS data.

This diffusion model demonstrates K^+ diffusion through PMO *via* mixed pathways. A good fit is achieved using diffusion coefficients of D_b = 1.5 × 10^{-17} cm^2 s^{-1} and D_{bg} = 2.5 × 10^{-14} cm^2 s^{-1} for bulk and grain boundary diffusion, respectively. Sole bulk diffusion is also simulated using D_b = 1.5 × 10^{-17} cm^2 s^{-1} for comparison. Both Fig. 4 and 5 clearly illustrate the increased depth of penetration with high grain boundary diffusivities. It should be noted that in these simulations, the grain boundaries are placed far enough apart that their individual concentration distributions do not overlap. This may not be the case in the experimental PMO, where there may be regions with grain boundaries in close proximity. This interaction could influence the average concentration along the thickness of the film. Furthermore, our model does not consider the effects of space charge layers.

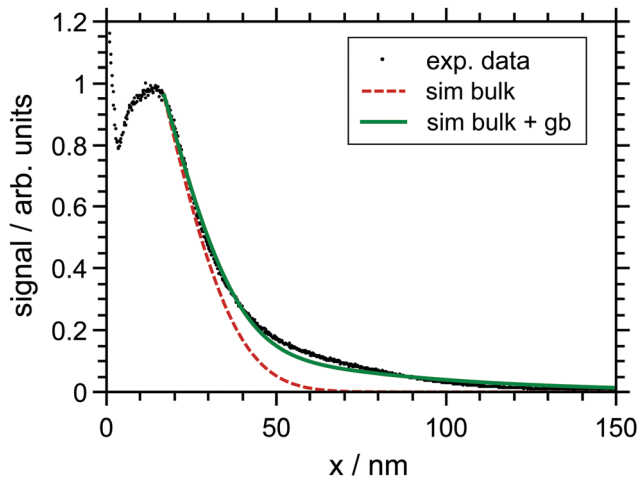

Fig. 5 Normalized concentration along the thickness of the film from ToF-SIMS (black), simulated mixed pathway diffusion (green), and simulated sole bulk diffusion with no grain boundary (red). The surface if the sample is at x = 0 nm.

4 Discussions

As pointed out above the transport of potassium into the PMO occurs under the sole influence of concentration gradients. Any possible gradient of the electric potential should be small at least inside the sample, although we cannot categorially rule out the possibility of potential steps in the interface region, *e.g.*, due to the redox pair K^+/K^0. Considering the observation that the sum of normalized signals for Pr^+ and K^+ is approximately constant in the bulk suggests that it is indeed K^+, which diffuses through the PMO. This is not a contradiction to the remark that most of the K^+ ions are neutralized by electron conduction towards the front side of the PMO. Most likely, the overall transport of potassium involves two aspects, (i) the neutralization of K^+ at the surface of the sample and (ii) another change of the effective oxidation state at the interface K/PMO. A similar change of the effective oxidation state of iron at the interface of a perovskite/vacuum has been reported by Opitz *et al.* in an XPS investigation of electrochemical water splitting.[33] Since potassium and praseodymium do not exhibit the same valency, the transport described above most likely involves a compensation by electron and/or hole transport and a change in the Manganese oxidation state.[34] In fact the material $Pr_{1-\delta}K_\delta MnO_3$ has indeed been investigated in some detail.[21] The result of our diffusion experiment corresponds to such a material, with the peculiarity that δ varies as function of depth into the material. The diffusion coefficients discussed above thus are considered effective diffusion coefficients. In the context of the classical model for grain boundary diffusion the situation operative in the current investigation most closely corresponds to Harrison's B case.[35] The HRTEM image in Fig. 3b reveals that the perovskite crystal structure is preserved

even in K-rich areas close to the interface. This observation supports our hypothesis that K occupies sites of the perovskite lattice. Due to its large ion radius, potassium is most likely substituting the praseodymium cations in the A site.

The analysis of grain boundary diffusion and its relation to bulk diffusion has received considerable interest.[31,36–41] The finding of this work, *i.e.*, the diffusion coefficient for grain boundary diffusion being approximately 3 orders larger than that for bulk diffusion, is in fact in line with numerous reports in the literature; for a recent review see ref. 42. On the other hand there are also reports of grain boundaries effectively hindering oxygen transport in yttria stabilized zirconia.[43] Ultimately, the macroscopic consequence of grain boundaries is believed to depend on many microscopic details, and therefore must most likely be examined for each sample separately.

5 Summary

The transport of potassium through praseodymium-manganese oxide (PMO) has been investigated by means of the charge attachment induced transport technique. *Ex situ* ToF-SIMS analysis provided bimodal concentration profiles of the potassium, which were attributed with two distinct transport pathways. This conclusion is supported by electron microscopy revealing the presence of twin boundaries at average spacing of 140 nm. Based on theoretical modeling, a good fit to experimental data was be achieved by assuming a bulk diffusion coefficient of $D_b = 1.5 \times 10^{-17}$ cm^2 s^{-1} and a larger grain boundary diffusion coefficient of $D_{gb} = 2.5 \times 10^{-14}$ cm^2 s^{-1}, assuming the grain boundary density similar to the microscopy data.

Acknowledgements

Financial support of this work by the Deutsche Forschungsgemeinschaft (DFG We 1330/17-1 and DFG Jo 348-10/1) is gratefully acknowledged. The simulations are based upon work supported as part of the NorthEast Center for Chemical Energy Storage, an Energy Frontier Research Center funded by the U.S. Department of Energy, Office of Science, Office of Basic Energy Sciences under Award Number DE-SC0012583. The computational resources were provided by the University of Michigan Advanced Research Computing. Stimulating discussions with Anneli Hein, Martin Schäfer, and Hui-Chia Yu are gratefully acknowledged.

References

1 L. Lu, C. Ni, M. Cassidy and J. T. S. Irvine, *J. Mater. Chem. A*, 2016, **4**, 11708–11718.
2 S. Raabe, D. Mierwaldt, J. Ciston, M. Uijttewaal, H. Stein, J. Hoffmann, Y. Zhu, P. Blöchl and C. Jooss, *Adv. Funct. Mater.*, 2012, **22**, 3378–3388.
3 (*a*) J. Suntivich, K. J. May, H. A. Gasteiger, J. B. Goodenough and Y. Shao-Horn, *Science*, 2011, **334**, 1380–1383; (*b*) Y. Matsumoto and E. Sato, *Mater. Chem. Phys.*, 1986, **14**, 397–426; (*c*) R. A. Rincon, E. Ventosa, F. Tietz, J. Masa, S. Seisel, V. Kuznetsov and W. Schuhmann, *ChemPhysChem*, 2014, **15**, 2810–2816; (*d*) J. O. Bockris and T. Otagawa, *J. Phys. Chem.*, 1983, **87**, 2960–2971.
4 A. Sawa, *Mater. Today*, 2008, **11**, 28–36.
5 C. Ye, J. Wu, G. He, J. Zhang, T. Deng, P. He and H. Wang, *J. Mater. Sci.*, 2016, **32**, 1–11.
6 I. C. Man, H.-Y. Su, F. Calle-Vallejo, H. A. Hansen, J. I. Martínez, N. G. Inoglu, J. Kitchin, T. F. Jaramillo, J. K. Nørskov and J. Rossmeisl, *ChemCatChem*, 2011, **3**, 1159–1165.
7 E. Bucher, *Solid State Ionics*, 2003, **157**, 39–44.
8 J. Mizusaki, H. Tagawa, K. Naraya and T. Sasamoto, *Solid State Ionics*, 1991, **49**, 111–118.
9 D. Varshney, I. Mansuri and N. Kaurav, *J. Phys.: Condens. Matter*, 2007, **19**, 246211.
10 M. B. Salamon and M. Jaime, *Rev. Mod. Phys.*, 2001, **73**, 583–628.
11 (*a*) T. Ishigaki, S. Yamauchi, K. Kishio, J. Mizusaki and K. Fueki, *J. Solid State Chem.*, 1988, **73**, 179–187; (*b*) S. Miyoshi and M. Martin, *Phys. Chem. Chem. Phys.*, 2009, **11**, 3063–3070.
12 M. Schäfer and K.-M. Weitzel, *Phys. Chem. Chem. Phys.*, 2011, **13**, 20112.
13 P. V. Menezes, J. Martin, M. Schäfer, H. Staesche, B. Roling and K.-M. Weitzel, *Phys. Chem. Chem. Phys.*, 2011, **13**, 20123.
14 S. Schulze, M. Schäfer, A. Greiner and K.-M. Weitzel, *Phys. Chem. Chem. Phys.*, 2013, **15**, 1481–1487.
15 V. Wesp, M. Hermann, M. Schäfer, J. Hühn, W. J. Parak and K.-M. Weitzel, *Phys. Chem. Chem. Phys.*, 2016, **18**, 4345–4351.
16 K. M. Weitzel, *Diffus. Found.*, 2016, **6**, 107–143.
17 L. Rossrucker, P. V. Menezes, J. Zakel, M. Schaefer, B. Roling and K.-M. Weitzel, *Z. Phys. Chem.*, 2012, **226**, 341–353.
18 J. Martin, S. Mehrwald, M. Schäfer, T. Kramer, C. Jooss and K.-M. Weitzel, *Electrochim. Acta*, 2016, **191**, 616–623.
19 D. Budina, J. Zakel, J. Martin, P. Menezes, M. Schäfer and K.-M. Weitzel, *Z. Phys. Chem.*, 2014, **228**, 609–627.
20 T. Kolling, A. Schlemmer, C. Pietzonka, B. Harbrecht and K.-M. Weitzel, *J. Appl. Phys.*, 2010, **107**, 14105.
21 Z. Jirák, J. Hejtmánek and K. Knížek, *J. Solid State Chem.*, 1997, **132**, 98–106.
22 M. Rajasekhar, P. Matheswaran and A. Subramania, *J. Environ. Nanotechnol.*, 2015, **4**, 51–54.
23 P. A. W. van der Heide, *Appl. Surf. Sci.*, 2006, **252**, 6456–6458.
24 P. A. W. van der Heide, *Nucl. Instrum. Methods Phys. Res., Sect. B*, 2002, **194**, 489–502.
25 A. B. Muñoz-García, A. M. Ritzmann, M. Pavone, J. A. Keith and E. A. Carter, *Acc. Chem. Res.*, 2014, **47**, 3340–3348.
26 R. A. De Souza and J. A. Kilner, *Solid State Ionics*, 1999, **126**, 153–161.
27 R. A. De Souza and J. A. Kilner, *Solid State Ionics*, 1998, **106**, 175–187.
28 R. A. De Souza, J. A. Killner and J. F. Walker, *Mater. Lett.*, 2000, **43**, 43–52.
29 M. A. Carpenter, R. E. A. McKnight, C. J. Howard and K. S. Knight, *Phys. Rev. B: Condens. Matter Mater. Phys.*, 2010, **82**, 094101.

30 H. Mehrer, *Diffusion in solids. Fundamentals, Methods, Materials, Diffusion-Controlled Processes*, Springer, 2007, vol. 155.
31 J. C. Fisher, *J. Appl. Phys.*, 1951, **22**, 74.
32 H.-C. Yu, M.-J. Choe, G. G. Amatucci, Y.-M. Chiang and K. Thornton, *Comput. Mater. Sci.*, 2016, **121**, 14–22.
33 A. K. Opitz, A. Nenning, C. Rameshan, R. Rameshan, R. Blume, M. Haevecker, A. Knop-Gericke, G. Rupprechter, J. Fleig and B. Kloetzer, *Angew. Chem., Int. Ed.*, 2015, **54**, 2628–2632.
34 J. Richter, P. Holtappels, T. Graule, T. Nakamura and L. J. Gauckler, *Monatsh. Chem.*, 2009, **140**, 985–999.
35 L. G. Harrison, *Trans. Faraday Soc.*, 1961, **57**, 1191.
36 A. D. Le Claire, *Br. J. Appl. Phys.*, 1963, **14**, 351–356.
37 I. Kaur, Y. Mishin and W. Gust, *Fundamentals of grain and interphase boundary diffusion*, John Wiley, 3rd edn, 1995.
38 Y. Mishin and C. Herzig, *Mater. Sci. Eng., A*, 1999, **260**, 55–71.
39 D. Gryaznov, J. Fleig and J. Maier, *Defect Diffus. Forum*, 2005, **237–240**, 1043–1048.
40 M. Palcut, J. S. Christensen, K. Wiik and T. Grande, *Phys. Chem. Chem. Phys.*, 2008, **10**, 6544–6552.
41 S. P. Harvey, R. A. de Souza and M. Martin, *Energy Environ. Sci.*, 2012, **5**, 5803–5813.
42 R. A. De Souza and M. Martin, *MRS Bull.*, 2009, **34**, 907–914.
43 R. A. de Souza, M. J. Pietrowski, U. Anselmi-Tamburini, S. Kim, Z. A. Munir and M. Martin, *Phys. Chem. Chem. Phys.*, 2008, **10**, 2067–2072.